TITLE

Effects of visual inputs on neural dynamics for coding of location and running speed in medial entorhinal cortex.

AUTHORS

Holger Dannenberg[1], Hallie Lazaro[1], Pranav Nambiar[1], Alec Hoyland[1], Michael E. Hasselmo[1]

INSTITUTIONAL AFFILIATIONS

[1]Center for Systems Neuroscience, Boston University, Boston, MA 02215, USA

ABSTRACT

Neuronal representations of spatial location and movement speed are important for a broad range of cognitive functions, including spatial self-localization and memory-guided navigation. Two possible speed signals, by theta frequency or by firing rate, have been hypothesized to provide the velocity signal needed for generating the spatially periodic grid cell firing pattern. However, which of these speed signals is utilized by the brain remains unknown. By manipulating visual inputs and analyzing the time-courses of evoked changes, we demonstrate that changes in spatial stability of grid cell firing correlate in time with changes in speed coding by local field potential theta frequency. In contrast, visual inputs do not affect speed coding by firing rate even if baseline firing rates are changed. Moreover, grid cells maintain a spatially periodic firing pattern, though less stable, in complete darkness. These data suggest that mice use an oscillatory speed signal to perform path integration.

INTRODUCTION

The spatially periodic firing of grid cells in the medial entorhinal cortex (MEC) (Fyhn et al., 2004, 2008; Hafting et al., 2005) is widely recognized as a neuronal correlate of memory-guided and/or self-motion-based spatial navigation (McNaughton et al., 2006). Based on that idea, computational models of grid cells including attractor network models (Burak & Fiete, 2009; Fuhs & Touretzky, 2006), oscillatory interference models (Blair et al., 2008; Burgess, 2008; Burgess et al., 2007; Hasselmo, 2008; Zilli & Hasselmo, 2010), hybrid models of attractor networks and oscillatory interference (Bush & Burgess, 2014), or probabilistic learning models (Cheung, 2016) suggest that grid cells integrate running direction and traveled distance to maintain a spatially periodic firing pattern. However, the source of both the direction signal and the speed signal are unclear. The direction signal has been attributed to the head direction

signal terminating in the MEC (Sargolini et al., 2006; Taube et al., 1990; Taube et al., 1990; Taube, 2007), but this does not match movement direction (Raudies et al., 2015). The analysis presented here focuses on the question of the dominant source of the speed signal which is also still under debate. One potential candidate for the speed signal is the linear modulation of firing rates in a subpopulation of context-invariant “speed cells” in the MEC (Kropff et al., 2015). However, such a speed signal by firing rate has been shown to be more heterogeneous than previously assumed (Hardcastle et al., 2017) and not accurate on sub-second-long time scales (Dannenberg et al., 2019). An alternative or complementary oscillatory speed signal is provided by the positive correlation between the local field potential (LFP) theta frequency and the running speed of an animal and/or the positive correlation between theta rhythmic firing frequency of theta modulated MEC neurons and the running speed of an animal (Hinman et al., 2016). Both the firing rate and rhythmicity running speed signals depend on self-motion cues, which include vestibular and proprioceptive signals (Chen et al., 2019; Tennant et al., 2018) and also moving sensory features such as optic flow (Campbell et al., 2018; Raudies et al., 2012; Raudies & Hasselmo, 2015). However, any path integration mechanism ultimately suffers from the accumulation of error over distance traveled or elapsed time (Kraus et al., 2015; Sreenivasan & Fiete, 2011) necessitating error correction by static environmental sensory inputs (Evans et al., 2016; Giocomo, 2016) such as visual landmark cues (Hafting et al., 2005) or environmental boundaries (Barry et al., 2007; Hardcastle et al., 2015) to maintain an accurate representation of relative self-location within a spatial environment. Experimental data from studies on rats support the hypothesized role of grid cells in performing self-motion based path integration and error correction by sensory cues: Self-motion-based signals such as head direction are necessary for grid cell firing (Winter et al., 2015), and grid cell firing persists during darkness with reduced spatial selectivity (Hafting et al., 2005) reflecting the loss of error correction by visual cues. In contrast, two more recent studies on mice reported a nearly complete loss of spatially periodic grid cell firing during complete darkness (Chen et al., 2016; Pérez-Escobar et al., 2016) suggesting a critical role for visual inputs on grid cell firing and presenting a challenge for current path integration models. However, visual cues appear to have been the only available source of sensory information in those experiments leaving the question open if and how visual inputs affect grid cell firing in mice under standard conditions which include other landmark features such as walls, auditory, and olfactory cues still available to the animal. Moreover, little is known about the time courses of changes in coding of location by grid cells and running speed by theta oscillations or firing rate (for instance during changes from light to darkness), although changes in grid cell firing, theta rhythmic dynamics, and speed

modulation of firing rates may underlie many cognitive functions on a behavioral time scale ranging from seconds to minutes. Moreover, we propose that testing for temporal correlations between grid cell spatial stability and the two proposed speed signals—by firing rate or theta oscillations—will help to identify the speed signal with the greatest influence on grid cell firing. Data presented in this study are relevant both for models of path integration and for our understanding of how visual inputs modulate the coding of location and running speed in the entorhinal cortex.

RESULTS

To study changes in neural dynamics after transitioning from foraging in an illuminated environment (light) to foraging in complete darkness (dark) and vice versa, we recorded single unit and local field potential (LFP) activity in mice freely exploring an open field environment during alternating light and dark epochs (**Fig. 1A**). We first studied if the absence of visual inputs in the dark condition changed the speed signal by LFP theta frequency. We found that the slope of the LFP theta frequency vs. running speed relationship was changed between light and dark conditions (t-statistic of interaction effect: 18.045, $p < 0.0000$, n = 15 mice) (**Fig. 1B**). In contrast, the theta amplitude vs. running speed relationship did not change significantly (t-statistic of interaction effect: 1.7343, $p = 0.0832$, n = 15 mice) (**Fig. 1C**). Average running speed during light was 11.6 ± 0.5 cm/s which slightly decreased after transition to dark by 0.89 ± 0.31 cm/s (7.7%) to 10.72 ± 1.4 cm/s (mean ± sem, $p = 0.0117$, n = 15 mice, Wilcoxon's signed rank test) (**Fig. 1D and Supplementary Fig. 1A**). Similarly, running acceleration also slightly decreased from 20.8 ± 1.9 cm/s^2 in the light condition by 1.7 ± 0.7 cm/s^2 (8.0%) to 19.1 ± 2.3 cm/s^2 in the dark condition ($p = 0.0070$, n = 15 mice, Wilcoxon's signed rank test) (**Fig. 1E**). We therefore examined if the observed decrease in the slope of the LFP theta frequency vs. running speed relationship might result from the decrease in running *acceleration* during darkness. If the decrease in slope is due to a decrease in running acceleration, there should be no change in the y-intercept of the LFP theta frequency vs. running *acceleration* between light and dark conditions. However, the y-intercept of the LFP theta frequency vs. running acceleration relationship did change significantly in darkness (t-statistic: 114.67, $p < 0.0000$, n = 15 mice, Student's paired t-test) (**Fig. 1F**)**.** Furthermore, if a decrease in acceleration causes the change, then there should be no change in the slope of the LFP theta frequency vs. running speed relationship between light and dark conditions if we restrict our analysis of speed tuning to time points where the running acceleration is constant. However, testing the relationship between LFP theta frequency vs. running speed only at time points when running acceleration was near

zero (0 ± 5 cm/s^2) resulted in speed tuning curves of LFP theta frequency (**Fig. 1G**) that looked nearly identical to the ones obtained without that restriction (Fig. 1B). These data demonstrate that the LFP theta frequency is directly modulated by running speed and that the observed change in the slope of the LFP theta frequency vs. running speed relationship in darkness is not an artifact of an underlying change in running behavior but instead directly reflects a change of visual inputs.

The LFP theta frequency vs. running speed relationship has been hypothesized to serve as a speed signal important for coding of location during self-motion-based navigation including path integration. Having established that the removal of visual inputs changes the speed signal by LFP theta frequency, we were further interested in the time-course of that change. We therefore analyzed sequential 10-sec blocks after transitioning from light to dark and vice versa. Averaging data from 73 sessions from 13 mice, we found that the time course of the change in LFP theta frequency vs. running speed relationship showed two components: an instantaneous change and a further exponential change at a time scale of tens of seconds (**Fig. 1H, I, K**). After removal of all visual inputs, LFP theta frequency shows an instantaneous decrease followed by a further exponential decay. Once the environment is illuminated again, LFP theta frequency shows an instantaneous increase followed by a further saturating exponential increase over tens of seconds. Analyzing the slopes of the LFP theta frequency speed tuning curves for sequential 10-sec blocks revealed that the observed exponential change in theta frequency over time was largely driven by a change in the slope of the theta frequency vs. running speed relationship (**Fig. 1J, L**), while the y-intercepts were only slightly—though significantly—lower during darkness ($t = 4.90$, $p = 3.6 \times 10^{-5}$, $n = 15$ time bins, Student's paired t-test) (**Supplementary Fig. 1B & C**).

Local field potential activity in the MEC primarily reflects the summed activity of synaptic inputs to the MEC, which is likely to be correlated with firing patterns of MEC neurons. Many neurons in the MEC show a theta rhythmic firing pattern and—similarly to the LFP theta frequency—the frequency of theta rhythmic firing increases with running speed (Hinman et al., 2016). In our data set, we identified a total of n = 342 neurons from 14 mice as theta modulated based on their autocorrelograms. We asked if and how theta rhythmic firing in these theta modulated MEC neurons is affected by removing and reinstating all visual inputs. Towards that aim we used an MLE approach (Climer et al., 2015) to fit a model of theta spiking rhythmicity to the observed spike train autocorrelations and identify the frequency and magnitude of theta

rhythmic firing in theta modulated MEC neurons in the light and dark conditions (see **Fig. 2A** for one example neuron). We first analyzed the relationship between the frequency of theta rhythmic firing and running speed. The results of this analysis show that the frequency of theta rhythmic firing increases with running speed in an illuminated environment (n = 340 neurons, **Fig. 2B**) as previously shown in rats (Hinman et al., 2016). Similar to the observed decrease in slope of the LFP theta frequency vs. running speed relationship, the slope of the frequency of theta rhythmic firing vs. running speed relationship decreased in complete darkness (**Fig. 2B**).

To study the time-course of changes in theta rhythmic firing, we next analyzed theta rhythmic firing in sequential 10-sec blocks after transitioning from light to dark and vice versa. In contrast to the exponential changes observed in the LFP theta frequency, the frequency of theta rhythmic firing decreased instantaneously with removal of all visual inputs and increased again instantaneously with reinstating all visual inputs (**Figs. 2C-E**). Interestingly, the theta rhythmic magnitude of the average autocorrelogram model across all 342 theta modulated neurons appeared higher during complete darkness compared to the light condition (**Figs. 2C & E**). The increased amplitude in the average across autocorrelogram models could either reflect an increase of theta rhythmic magnitude on the single cell level or an increased synchrony across neurons on the population level. To distinguish between these two possibilities, we analyzed changes in theta rhythmic firing on the single cell and population level for different running speeds (immobility defined as running speed < 3 cm/s, 5-10 cm/s, 10-15 cm/s, 15-20 cm/s, 20-25 cm/s) (n = 339 neurons, **Fig. 2F**). To our surprise, we found that neurons continued to fire rhythmically during immobility periods in both light and dark conditions. However, theta rhythmic frequencies varied largely across neurons within a wide range of theta frequencies (4-12 Hz) during immobility. As soon as the mouse started running, however, theta rhythmic firing synchronized across neurons around a narrower theta frequency range of 6-10 Hz. Interestingly, theta dynamics showed a different development between light and dark conditions (**Fig. 2F-I**). The magnitude of theta rhythmic firing increased with running speed during the light condition, but decreased with running speed during the dark condition (notice brighter yellow peaks in **Fig. 2F**). Similarly, the frequency of theta theta rhythmic firing increased with running speed during the light condition, but less so during the dark condition (**Fig. 2F**).

In order to quantify these changes in theta rhythmic firing on the population level, we identified individual neurons with statistically significant rhythmic modulation of firing per running speed condition (alpha = 0.1). In the light condition, we found 206 out of 339 neurons with statistically

significant rhythmic firing during immobility. This number sharply increased to 298 with the onset of running, but then steadily decreased to 270, 256, and 241 for higher running speeds. In the dark condition, the number of rhythmically firing neurons showed a similar sharp increase with the onset of running (from 187 to 313 neurons). In contrast to the light condition, however, the number of rhythmic neurons during darkness further increased to 322, 326, and 328 out of 339 neurons with higher running speeds (**Fig. 2G**). These numbers demonstrate that the ensemble of theta rhythmic firing neurons decreased with running speed in the light condition, but increased to ceiling during the dark condition (**Fig. 2G**) contributing to the stronger synchrony of theta rhythmic firing observed on the population level (**Fig. 2F**).

We next quantified the changes in theta rhythmicity magnitude and theta rhythmic frequency in the subset of rhythmically firing neurons per running speed condition and comparing light vs. dark conditions. Theta rhythmicity magnitude increased with running speed during light, but decreased with running speed during dark resulting in larger differences between light and dark conditions for higher running speeds. Consequently, these differences in theta rhythmicity magnitude reached statistical significance for running speeds higher than 15 cm/s (**Fig. 2H,** Kolmogorov-Smirnov test, $p < 0.001$ for running speeds > 15 cm/s, see Fig. 2H for exact p-values). Notably, the amplitudes of the average autocorrelogram models across all cells were very similar between light and dark conditions (**Fig. 2F,** third row) despite the observed differences in the magnitudes of theta rhythmicity on the single cell level (**Fig. 2H**). These data suggest that—during darkness— higher synchrony across MEC neurons on the population level counterbalances the lower magnitude of theta rhythmicity on the single cell level resulting in little change on the LFP level. In contrast, changes in theta rhythmic frequencies with higher running speed correlated with changes in LFP theta frequency in both light and dark conditions (**Figs. 1B & 2I**); theta rhythmic frequencies increased with running speed and more so in the light compared to the dark condition (**Fig. 2I**). Consequently, the differences between light and dark became more prominent and statistically more significant with higher running speeds (**Fig. 2I**, Kolmogorov-Smirnov test, $p < 0.05$ for immobility periods, $p < 0.0001$ for running speeds > 5 cm/s, and $p < 0.00001$ for running speeds > 10 cm/s, see Fig. 2I for exact p-values).

Motivated by the differences in LFP activity during light and dark conditions, we asked if these changes were accompanied by changes in firing rates of MEC neurons. We therefore first asked if and how the removal and reinstating of visual inputs affected baseline firing rates in MEC neurons. We found striking differences in baseline firing rates between light and dark epochs

among a wide variety of MEC neurons including speed cells, head direction cells, grid cells, boundary-vector cells and interneurons **(Fig. 3A & B; Supplementary Fig. 2)**. In general, changes in firing rates of MEC neurons could be positive or negative with positive changes being observed ~4 times more frequently than negative changes (139 out of 1205 or 11.5% positively modulated neurons; 32 out of 1205 or 2.7% negatively modulated neurons at significance level alpha = 0.05; data from 15 mice). In both cases, changes in firing rate after transition from light to dark or from dark to light occurred instantaneously (**Fig. 3C & D**).

One possible explanation for the observed changes in firing rates can be a binary change in the visibility of landmark cues, i.e. the presence or absence of visual information about the animal's spatial surroundings. Alternatively, changes in firing rates could be driven by changes in net excitatory drive from areas in the visual cortex due to changes in retinal stimulation independent of any gain or loss of information about the animal's spatial surroundings. To distinguish between these two alternative hypotheses, we analyzed data from optogenetic control experiments in a subset of two mice, in which mice carried a light fiber attached to their headstage with the fiber tip approximately 1cm above the animal's head. Green laser light (561nm, 1mW) was emitted from the tip of that light fiber and illuminated the head and immediate surroundings of the animal's head. While being visible to the animal as an egocentrically stationary spot of light, it was too weak to illuminate the open field environment and thus did not contribute to the visibility of distal visual cues useful for navigational purposes (e.g. walls or the cue card of the open field arena). Nevertheless, we found strong effects of that kind of visual point stimulation on firing rates of five MEC neurons from two mice during foraging under the light condition (**Fig. 3E & F**). Four out of those five neurons showed positive modulation by the egocentrically stationary spot of laser light, and one showed negative modulation. The effects of presenting an egocentrically stationary visual stimulus during the light condition on baseline firing rates of MEC neurons resembled the effects of transitioning from the dark to the light condition. Overall, increased baseline firing rates due to stronger retinal stimulation were ~4 times more likely to be observed than decreases in firing rates. In summary, these data demonstrate that the changes in retinal stimulation due to changes in the amount of spatially non-informative light hitting the retina after transitioning from dark to light and vice versa are sufficient to explain the observed changes in firing rates of MEC neurons.

We next turned to the analysis of the hypothesized speed signal by firing rate, in particular "speed cells" in the MEC (Kropff et al., 2015) and asked if the speed modulation of firing rates in

MEC neurons is changed in complete darkness. Speed cell firing has previously been reported to be affected by removal of visual inputs and this change in speed cell firing has been interpreted as a change in the hypothesized speed signal by speed cells, which has further been indicated to underlie changes in grid cell firing and path integration during darkness (Chen et al., 2016; Pérez-Escobar et al., 2016). As shown above, many neurons change baseline firing rates during darkness and many speed cells show conjunctive coding properties which may be changed in complete darkness (Hardcastle et al., 2017; Hinman et al., 2016). To our knowledge, previous analyses of firing rate modulation by running speed have not been corrected for changes in baseline firing rates or changes in conjunctive coding properties. In this study, we therefore 1) corrected for effects on baseline firing rates by random spike deletion to match the number of spikes across light and dark conditions, 2) applied a linear-nonlinear (LN) model (Hardcastle et al., 2017) to identify speed modulated neurons and correct for conjunctive coding properties, such as conjunctive coding for position, head direction, and LFP theta phase. The LN-model provides an unbiased method for identification of significantly speed modulated neurons and for quantification of their speed response curves (Hardcastle et al., 2017). The firing rates of n = 142 neurons out of 425 cells from 14 mice showed significant modulation by running speed in either the light or the dark condition. Consistent with previous reports, speed modulation of firing rates was heterogenous (**Fig. 4A**) (Dannenberg et al., 2019; Hardcastle et al., 2017; Hinman et al., 2016). Hierarchical clustering of speed cells resulted in two main clusters of 119 positively and 23 negatively modulated neurons (**Fig. 4B**). We did not find biologically significant differences in the speed tuning of firing rates comparing light vs. dark conditions in positively or negatively modulated MEC neurons (**Fig. 4C**). Likewise, speed scores (Pearson's correlation coefficient between firing rate and running speed) of all speed modulated neurons were not significantly changed between light and dark conditions on the population level ($p = 0.6722$, $n = 142$, Kolmogorov-Smirnov test) (**Fig. 4D**) and were highly correlated between light and dark conditions on the single cell level ($R = 0.87$) **(Fig. 4E**). Moreover, conjunctive coding of position, head direction and theta phase was unchanged (**Fig. 4F**). In summary, our data on speed modulation of firing rates in MEC neurons demonstrate that a potential speed signal by speed cells in the MEC depends neither on visual inputs nor visibility of landmark cues. Furthermore, speed modulation of firing rates is indifferent to changes in baseline firing rates or changes in conjunctive coding properties.

While grid cells have been reported to show stable grid cell firing during complete darkness in rats (Hafting et al., 2005), two recent studies in mice showed a strong reduction in the

hexagonal symmetry of grid cell firing during complete darkness (Chen et al., 2016; Pérez-Escobar et al., 2016) challenging computational models of grid cells and path integration. To test if this discrepancy is due to a difference between species or due to differences in the experimental settings, the focus in this study was on selectively eliminating visual inputs only, while leaving other environmental and/or sensory cues such as walls or odors and auditory cues potentially present in the testing arena intact. We first tested if grid cell firing can emerge in complete darkness. We therefore introduced mice to the familiar open field arena during complete darkness (the experimenter was wearing night-vision goggles) and recorded grid cells during the initial dark session and a following light and dark session (10-20 min duration each). We found that spatial periodicity of grid cell firing was low—but not completely eliminated—in the initial dark session and then strongly increased during the first light session **(Fig. 5A & B)**. Interestingly, after this initial orientation, spatial periodicity of grid cell firing decreased again after removal of visual inputs, but remained significantly higher than in the initial dark session (Chi-square = 10.89, $p = 0.0043$, $n = 9$ cells from two mice, Friedman test; post hoc tests revealed $p < 0.05$ comparing initial dark and light, and initial dark and second dark sessions). We next aimed to study the change in grid cell spatial firing patterns after transitioning from light to dark in more detail. Towards that aim, we recorded grid cells during alternating light/dark epochs, always beginning with a light epoch followed by a dark epoch. 27 cells from six mice were identified as grid cells based on their grid scores (see Methods). To compare spatial firing properties of grid cells between light and dark conditions, we concatenated all light and dark sessions to compute firing rate maps for light and dark conditions. We found that grid cell field centers remained stable, but grid fields appeared wider during complete darkness (**Fig. 5C**). Quantification of spatial periodicity and spatial precision of grid cell firing by computing grid scores and spatial information (see Methods) revealed a significant decrease in both spatial periodicity and spatial precision of spike locations (**Fig. 5D & E**). However, firing rate maps are the results of integrating firing rates of grid cells over long time periods, thereby measuring only spatial variability, but not spatio*temporal* variability of grid cell firing. This distinction becomes important when considering two alternative hypotheses with regard to the underlying cause for the observed broadening of grid fields in complete darkness. Grid fields could appear wider because grid cells fire over a longer distance throughout a single grid field traversal. Alternatively, grid fields could appear wider because grid cell firing becomes less stable at the level of single grid field traversals. To distinguish between these two alternative hypotheses, we computed the spatiotemporal correlation between the observed firing rate over time and the firing rate predicted by the animal's location at any given point in time and the associated value

in the firing rate map at that location. The results show a significant reduction in spatiotemporal correlation during complete darkness (**Fig. 5F**) supporting the hypothesis that grid fields in the firing rate appear broader because the spatiotemporal accuracy of grid cell firing is reduced.

Our data set included data on n = 7 grid cells from three mice recorded over an exceptionally long time period across multiple days. These data provided sufficient statistical power and sufficient sampling of the environment to analyze the time courses of the observed reductions in spatial periodicity, spatial selectivity and spatiotemporal stability of grid cell firing after transitions from light to dark and vice versa. Towards this goal, we first computed firing rate maps for each of the 10-sec bins of activity to analyze the time course of spatial periodicity quantified by the grid score (**Fig. 6A & B**). Second, we computed the spatial correlations between the firing rate maps of the 10-sec binned data and the overall firing rate map for the light condition (**Fig. 6C**). Third, we computed the spatiotemporal correlation for each of the 10-sec bins (**Fig. 6C**). We found an exponential change in spatial periodicity of grid cell firing (**Fig. 6B**), spatial correlation (**Fig. 6C**), and spatiotemporal correlation (**Fig. 6D & E**) over tens of seconds after transitions from light to dark and vice versa. Intriguingly, the time course of changes in spatiotemporal correlation showed a remarkable similarity to the time course of changes in the slope of the LFP theta frequency vs. running speed relationship (**Fig. 6F**). Taken together, these data demonstrate that the representation of space by grid cell firing is correlated to the speed signal by LFP theta frequency and that both of these signals undergo plastic changes at a behavioral time scale of tens of seconds.

DISCUSSION

Data presented in this study show that visual inputs affect neural dynamics underlying the coding of location and running speed in the MEC. These effects include changes in LFP theta rhythmicity as well as changes in baseline firing rates, changes in theta rhythmic firing, and changes in spatial periodicity of grid cell firing in response to visual inputs. By analyzing the time courses of changes in those variables, we found that spatial periodicity of grid cell firing and LFP theta frequency showed an instantaneous component and a slower exponential component of change. In contrast, changes in baseline firing rates and theta rhythmic firing only showed the instantaneous component. Furthermore, speed modulation of firing rates showed no change after transitions between light and dark conditions. Our data demonstrate that changes in the speed signal from LFP theta frequency is in concert with changes in the spatial stability of grid cells. Moreover, coding of location by grid cells and running speed by LFP theta frequency

showed changes at a behavioral time scale of tens of seconds. Such changes in response to changes in sensory input are longer than previously addressed by theoretical and computational models of grid cell firing. Lastly, we report changes in the running speed-dependent population dynamics of theta rhythmic MEC neurons upon changes in visual inputs. In both the light and dark condition, theta rhythmic neurons become more synchronized with the onset of running. However, synchronization across neurons is stronger during darkness, while frequency and magnitude of theta rhythmic firing of individual neurons increase significantly more with running speed during the light compared to the dark condition.

It has previously been proposed that disruption of speed signals may cause disruption of spatially periodic grid cell firing in the MEC. Computational models of grid cell firing and path integration require a linear speed signal (Burak & Fiete, 2009; Burgess, 2008; Burgess et al., 2007; Fuhs & Touretzky, 2006; McNaughton et al., 2006). Two candidates for such a speed signal terminating in the MEC have been proposed: a speed signal by firing rate, most clearly present in a subpopulation of “speed cells” showing context-invariant positive and linear speed tuning curves (Kropff et al., 2015); and an oscillatory speed signal by changes in LFP theta frequency or by changes in the theta rhythmic firing frequency of individual MEC neurons (Burgess, 2008; Hinman et al., 2016). Both speed signals can change in response to changes of the size and shape of the environment (Munn et al., 2020), as do grid cells (Barry et al., 2007; Krupic et al., 2015). Both speed signals may arise from the medial septum/diagonal band of Broca (MSDB) (Fuhrmann et al., 2015; Hinman et al., 2016; Justus et al., 2016) and contribute to self-motion-based linear distance estimation in the MEC (Jacob et al., 2017). However, speed modulation of firing rates is inaccurate at sub-second long time scales (Dannenberg et al., 2019) and the use of longer integration time windows has been shown to be insufficient for spatial periodicity of grid cell firing in a computational model of grid cell firing (Dannenberg et al., 2019).

The theta oscillatory speed signal also depends on the MSDB (Chrobak et al., 1989; Dannenberg et al., 2015; Givens & Olton, 1994; Hinman et al., 2016; Lawson & Bland, 1993) and pharmacological inactivation of MSDB neurons strongly reduces both theta oscillations and spatial periodicity of grid cell firing in the MEC (Brandon et al., 2011; Koenig et al., 2011). Furthermore, passive transportation of rats reduces theta oscillatory power and abolishes both spatially periodic grid cell firing and the speed signal by LFP theta frequency (Winter et al., 2015). Likewise, pharmacological inactivation of the vestibular system or preventing linear/translational head movements in a virtual reality setup abolish the modulation of LFP

theta frequency by running speed and are associated with a decrease in the spatial information score and an increase in grid scale (Chen et al., 2018; Jacob et al., 2014). Interestingly, the increase in grid scale observed during path integration on a circular track is associated with a change in LFP theta oscillations, but not with a change in the firing patterns of speed and head direction cells (Jacob et al., 2019). Taken together, these data suggest a dominant role of theta frequency modulation by running speed in generating the spatially periodic grid cell firing pattern.

However, the relative importance of the speed signal by firing rate on the one hand and the oscillatory speed signal by theta oscillations on the other hand for grid cell firing has not been explicitly tested so far. In order to test the relative importance of both speed signals, we took advantage of the disruption of spatially periodic grid cell firing caused by the absence of visual inputs and included the time domain into our analysis. Similar to the reasoning underlying the concept of Granger causality, we argued that a change in the speed signal driving path integration of grid cell firing should correlate in time with the changes in grid cell firing. However, if changes in the speed signal in question are uncorrelated to changes in grid cell firing, we can exclude a causal contribution of that potential speed signal to grid cell firing. In order to analyze the time course of grid cell stability over time after transitions between light and dark, we took advantage of long-term recordings of the same grid cells over multiple days providing us with sufficient statistical power. Intriguingly, changes in spatial stability of grid cell firing showed an instantaneous component and a slow exponential component at a behavioral time scale of tens of seconds after transitions between light and dark conditions. Notably, the observed exponential component in changes of grid cell spatially periodic firing is validated by an earlier report by Pérez-Escobar et al. (2016) although they reached different conclusions. We next tested if a change in the potential speed signal by firing rate may underlie the observed change in spatial stability of grid cell firing. However, the speed modulation of firing rates during complete darkness may show heterogeneous and multiplexed speed modulation of firing rate (Hardcastle et al., 2017) as well as changes in baseline firing rates due to loss of retinal stimulation and excitatory inputs from visual cortex (Campbell & Giocomo, 2018). We therefore corrected for differences in the number of spikes between light and dark epochs. We further corrected for multiplexed or conjunctive coding properties by computing speed response curves using a linear-nonlinear model (Hardcastle et al., 2017). After correcting for changes in baseline firing rates and conjunctive coding properties, we found that visual inputs had no impact on the speed modulation of firing rates in MEC neurons.

We next turned to the analysis of the time courses of changes in the two oscillatory speed signals, namely the speed signal by LFP theta frequency and the speed signal by theta rhythmic firing frequency. Intriguingly, the time course of changes in LFP theta frequency matched the time course of changes in grid cell spatial stability (Fig. 6F). In contrast, changes in theta rhythmic firing frequency showed only the instantaneous component of change (Fig. 2). These data on the parallel time course of changes in LFP theta and grid cell stability suggest that grid cells may depend more on the mean attractor state of rhythmic firing in the MEC reflected by the LFP theta signal than the rhythmic firing of individual neurons. Alternately, the exponential change in LFP theta may reflect a slow change in an oscillatory speed signal arising from other cortical structures such as the medial septum which has been demonstrated to be critical for both LFP theta and grid cell firing (Brandon et al., 2011; Koenig et al., 2011). Future studies are needed to address the question how theta rhythmic firing of MEC neurons can change more rapidly than the overall mean response in the LFP signal. Notably, the average frequency of theta rhythmic firing is higher than the average LFP theta frequency and we found variability in the range of theta rhythmic firing frequencies across neurons indicating that rhythmic firing of MEC neurons is only loosely coupled to the LFP theta frequency. Moreover—in contrast to LFP theta rhythmicity—theta rhythmic firing persists during immobility, though significantly less synchronous across neurons. The observed changes in theta rhythmic firing frequency at the single cell and population levels also provide a possible explanation for why the LFP theta amplitude vs. running speed relationship is not changed during complete darkness. During darkness, movement-related theta rhythmicity magnitude is decreased on the single cell level, while theta synchronicity across neurons is increased on the population level. These two effects would influence the LFP theta amplitude in opposite directions and thus may cancel each other out.

The observed changes in coding of running speed and location during complete darkness may be attributed to either a loss of visual cues for navigational purposes or alternatively to a net decrease in excitatory drive from areas in the visual cortex due to the lack of retinal stimulation (Campbell & Giocomo, 2018). In order to distinguish between these two possibilities, we took advantage of control data from an optogenetic study (Dannenberg et al., 2019), where a visible bright spot of light was moving geostationary to the animal without further illuminating the environment. During this manipulation, the amount of light hitting the retina increased without changing the visibility of static visual landmark cues. This perturbation resulted in very similar

changes of firing rates in MEC neurons as observed during the light vs. dark paradigm (Fig. 3). Importantly, changes of firing rates and theta rhythmic firing frequency occurred instantaneously upon changes in visual inputs (Figs. 2D and 3B & D). These data suggest that changes in firing rates and theta rhythmic firing frequency are primarily driven by changes in net excitatory input from visual cortex and do not reflect changes in the perception of the spatial aspects of the environment. We conclude that a lack of visual cues contributes to error accumulation in the path integration system. However, our data oppose previous proposals that changes in baseline firing rates of speed cells reflect the lack of information from visual cues. Instead, our data suggest that changes in baseline firing rates of speed cells are driven by changes in retinal stimulation or levels of brightness in the environment, while the modulation of firing rates by running speed—the actual speed signal by firing rate—is unaltered by changes in illumination or presence or absence of visual cues. Taken together, data presented in this study argue against a role of speed modulation of firing rates as speed signals for path integration and/or grid cell firing. In contrast, we found a striking correlation of changes in the LFP theta frequency vs. running speed relationship with changes in spatiotemporal accuracy of grid cell firing and hexagonal symmetry of grid cell firing. These data argue in favor of computational models of grid cell firing and path integration using an oscillatory speed signal by changes in LFP theta frequency (Burgess, 2008; Burgess et al., 2007; Hasselmo, 2008). This also suggests that individual neuron spiking may respond more rapidly than a slower mean population response of attractor dynamics underlying grid cell firing changes during the transitions.

Two recent studies on freely moving mice reported a major disruption of spatially periodic grid cell firing in the absence of visual cues (Chen et al., 2016; Pérez-Escobar et al., 2016). These findings questioned the role of grid cells for path integration-based navigation (Gil et al., 2018; Jacob et al., 2019) and are at odds with previous reports on grid cells in rats (Hafting et al., 2005) as well as results from studies using virtual reality demonstrating that physical motion has a greater influence on grid cell firing in mice than visual inputs (Campbell et al., 2018; Chen et al., 2019; Tennant et al., 2018). It remains controversial, however, if those discrepancies reflect a species difference between mice and rats or a difference in the experimental conditions. Critical to the interpretation of the studies carried out by Chen et al. (2016) and Pérez-Escobar et al. (2016), their studies carefully removed olfactory, auditory, and tactile cues in addition to the manipulation of visual cues to leave the animals completely disoriented, and impeding the selective study of visual inputs on spatially periodic grid cell firing. In this study, we therefore selectively manipulated visual inputs leaving other static environmental and sensory cues such

as walls, auditory cues, and potential olfactory cues unaltered. During this more selective manipulation, grid cells in the MEC persisted during complete darkness but showed reduced spatial selectivity. Our results further show that grid cell spatial periodic firing was reduced significantly more when mice were introduced to the test environment in complete darkness. These data suggest that grid cell firing needs to be initially anchored to a cognitive map and that this initial anchoring or orientation under standard testing conditions largely depends on the presence of static visual cues. However, once the animals have oriented themselves in the environment and grid cells have been anchored to a cognitive map, grid cell firing can be maintained by path integration even in the absence of visual information—though with decreasing spatial stability due to the absence of error correction by visual cues. Taken together, these data suggest that vestibular signals and proprioceptive feedback as well as external geometrical cues are dominant factors maintaining the orientation, scale, and phase of grid cell firing fields, while visual cues are used for refining a self-motion-based cognitive representation of self-location.

In summary, the time courses of changes in grid cell hexagonal symmetry, spatially selective firing, and spatiotemporal correlation caused by changes in visual inputs strongly resembled the time course of changes in speed tuning of LFP theta frequency (Fig. 6F). In contrast, neither changes in baseline firing rate, nor changes in theta rhythmic firing frequency showed the slow exponential component of change after transitioning from light to dark or vice versa. Furthermore, speed modulation of firing rates remained unaltered between light and dark conditions. These data suggest that the hypothesized oscillatory speed signal by LFP theta frequency may be more important for grid cell firing than a hypothesized speed signal by firing rate. Theta signals within the hippocampal formation have been suggested to not only reflect alterations in sensorimotor integration and/or the flow of sensory input, but also distinct cognitive operations (Hinman et al., 2011). Interestingly, we observed not only a slow exponential *decay* of spatial stability of grid cell firing upon removal of visual inputs, but also a slow saturating exponential *increase* in grid cell stability after reinstating illumination of the environment. Such a slow component at a time scale of tens of seconds after each transition between light and dark conditions suggest that the representation of space in a cognitive map is updated continuously at a behavioral time scale and more malleable than previously acknowledged.

METHODS

Subjects. Data were collected from a total of 17 adult 3-6 month old male mice (*mus musculus*) of wildtype and transgenic backgrounds (Wildtype, C57Bl/6J; ChAT-IRES-Cre, B6;129S6-Chat$^{tm2(cre)Lowl}$/J; PV-IRES-Cre, B6;129P2-Pvalb$^{tm1(cre)Arbr}$/J). Experimental PV-IRES-Cre mice were homozygous and experimental ChAT-IRES-Cre mice were heterozygous. All experimental procedures were approved by the Institutional Animal Care and Use Committee for the Charles River Campus at Boston University. Mice underwent surgery for implantation of 2 movable tetrodes targeting the superficial layers of the MEC in the left hemisphere. For the purpose of additional experiments not reported in this study, mice also underwent rAAV injections of Archaerhodopsin T or GCaMP6f into the medial septum and light fiber implantation targeting the medial septum (Dannenberg et al., 2019). No differences were observed between wildtype or transgenic mice. Prior to surgery, mice were housed in Plexiglas cages together with their siblings. After surgery, mice were separated for individual housing and maintained on a reversed 12-h light/12-h dark cycle. Mice were habituated to the experimenter and testing room before the start of all experimental procedures.

Surgery for microdrive implantation in mice. Mice were injected with buprenorphine (0.1-mg/kg, s.c.) and atropine (0.1-mg/kg, i.p.), and chronically implanted under isoflurane anesthesia with 8-channel Axona microdrives (Axona, St. Albans, UK) carrying two movable tetrodes targeting the superficial layers of the dorsal MEC in the left hemisphere. One ground screw was implanted above the cerebellum, five anchoring screws were positioned across the skull, and a craniotomy was performed for implantation of the microdrive, 0.5-mm anterior to the edge of the transverse sinus and 3.4-mm lateral to the midline. Tetrodes were then implanted with a 6° polar angle and lowered 1-mm into the brain. The microdrive was secured to the skull with dental cement. Animals were given buprenorphine (0.1-mg/kg, i.p.), enrofloxacin (7.5-mg/kg, i.p.), and ketoprofen (3-mg/kg, i.p.) during a 5-day postsurgical care period and allowed one week in total to fully recover after surgery before the start of recordings.

In vivo electrophysiological recordings. Before implantation, impedance of tetrodes (17-µm platinum wires, California Fine Wires) was adjusted by electroplating to < 150-kOhm. Tetrodes were lowered daily by 50-µm until the abundance of spikes and the presence of theta rhythmic cells in test recordings indicated that tetrode tips were located near or within the superficial cell layers of the MEC. Neural signals were pre-amplified by unity-gain operational amplifiers located on each animal's head (head stage) and AC-wire-coupled to an Axona recording system (Axona Limited, St. Albans, UK). Spikes were threshold-detected and recorded at 48-kHz. The

LFP signal was recorded single-ended with the ground screw as reference at 4800-Hz. Position and head direction of mice were tracked with headstage-mounted invisible infrared LEDs at 50-Hz. Spikes were clustered into single units using spike clustering software (DacqUSB/Tint, Axona, St. Albans, UK). Further offline analyses were performed using MATLAB (MathWorks, Natick, MA, USA) and RStudio software packages.

Behavior during light and dark conditions. All recordings were performed while animals foraged for randomly scattered small pieces of Froot Loops (Kellog Company, Battle Creek, MI, USA) in a 1m square open-field arena with 60-cm high black walls and a white letter size cue card at one wall. Recordings were performed during alternating epochs of open field illumination (light) and complete darkness (dark). Alternating epochs of recordings in light and darkness could vary in duration between 30 seconds and 30 min; most experiments used 3-min alternating epochs allowing high statistical power due to multiple repetitions from light to darkness in each session. A typical recording session lasted 40-60 min. A ceiling light provided full illumination of the open field during the light condition. For complete darkness the ceiling light was turned off. All other possible light sources in the room had been eliminated and the open field was fully shielded from any remaining light (e.g. door slits) by a black curtain. Tracking of position and head direction was achieved by using invisible infrared LEDs. Experiments with alternating epochs of light and dark began with the light condition. Experiments with a dark-light-dark paradigm started in complete darkness. For those experiments, mice were brought into the room, plugged in and introduced into the arena during complete darkness by an experimenter wearing night vision goggles.

Histology. After the end of electrophysiological data collection, animals were deeply anaesthetized by isoflurane or i.p. injection of Euthasol (390-mg/kg), followed by electro-lesions (20-µA, 16s) through one channel of each tetrode and subsequent transcardial perfusion with saline followed by 10% buffered formalin (SF100-4, ThermoFisher Scientifc). Brains were extracted and stored in fixative for one day. Cresyl violet staining was performed on 50-µm sagittal slices of MEC to visualize tetrode tracks and confirm positions of recording sites in the MEC.

Data analysis.

Computation of running speed and firing rate signals. The animal's running speed was estimated by applying a Kalman filter to the positional data obtained from the video tracking

sampled at 50-Hz (Fyhn et al., 2004; Hinman et al., 2016; Kropff et al., 2015). To obtain an instantaneous firing rate signal matching the sampling rate of the behavioral tracking, we calculated the firing rate as the number of spikes per video frame period (20-ms) and smoothed this signal with a 125-ms Gaussian filter.

Speed score. The speed score was calculated as the Pearson's product moment correlation between instantaneous firing rate and running speed (Kropff et al., 2015).

LFP theta rhythm. LFP data were down-sampled to 600-Hz and power spectral density analyses were performed using custom written MATLAB scripts and the FieldTrip toolbox (Oostenveld et al., 2011). A theta frequency range was determined for each session based on the range of the theta peak in the power spectral density plot (Dannenberg et al., 2019). The LFP signal was then band-pass-filtered at this theta frequency range with a third order Butterworth filter, and the instantaneous theta amplitude and phase were determined via a Hilbert transform. The instantaneous theta frequency could then be inferred from the instantaneous phase. To analyze changes in the LFP theta frequency vs. running speed relationship over time, we first down-sampled the LFP theta frequency to 50-Hz in order to match the temporal binning of the behavioral tracking. We next sectioned data into 10-sec blocks after transitions between light and dark and pooled data from all sessions and all mice (Fig. 1I). For each of those 10-sec blocks of data, a speed tuning curve of LFP theta frequency was computed at 1-cm/s resolution and the slope and y-intercept of the linear regression curve were determined (Fig. 1J). The same analysis as described above was applied to 10-sec blocks around the transition points from light to dark or from dark to light (Figs. 1K, L).

Theta rhythmic firing**.** We used maximum likelihood estimation (MLE) of a parametric model of the lags within the spike time autocorrelogram to analyze theta rhythmic firing, which has been proven a more sensitive and statistically rigorous method than traditional measures of spike time autocorrelogram features (Climer et al., 2015). In particular, this model allowed us to statistically test significance of theta modulation in MEC neurons and compare theta rhythmic firing frequency and theta rhythmicity magnitude on a single cell level between light and dark conditions. The model tested for rhythmic firing in the frequency range between 1-13 Hz. For the analysis of the relationship between theta rhythmic firing and running speed (Fig. 2), we first identified continuous temporal epochs larger than 400-ms, in which the running speed of the animal varied less than ± 4-cm/s. We next sorted these epochs according to the average running speed during the epochs into 1-cm/s bins from 1-cm/s to 29-cm/s and used the MLE approach to fit an autocorrelogram model to each of those epochs. For each neuron and running speed bin, an average autocorrelogram was computed across autocorrelograms for

each epoch. The maximal run time for the theta rhythmic firing vs. running speed analysis on the research computing cluster was set to two weeks resulting in the successful analysis of 340 out of 342 neurons. For the analysis of the time course of changes in theta rhythmic firing after transition from light to dark or from dark to light, the first two minutes after the transition were sectioned into 10-sec blocks (n = 342 neurons, Fig. 2D). Alternately, 10-sec blocks around the transition points from light to dark or from dark to light were analyzed (n = 342 neurons, Fig. 2E). For each neuron, an autocorrelogram model was fitted to each of those 10-sec blocks of data using the MLE approach. For each of those 10-sec blocks of data, the average theta rhythmic firing frequency across neurons could then be computed from the peaks of the average autocorrelogram model across neurons by taking the inverse of the first peak in the autocorrelogram model. To analyze running speed-dependent theta rhythmic firing on the population level, we first identified continuous epochs of running speed within the ranges of 0-3 cm/s (immobility), 5-10 cm/s, 10-15 cm/s, 15-20 cm/s, and 20-25 cm/s. We next used the MLE approach to model an autocorrelogram for each running speed bin of each neuron. Neurons with sufficient number of spikes to compute an MLE-modeled autocorrelogram in at least one of the running speed bins were included into the analysis (n = 339 neurons).

Computation of firing rate maps. Occupancy-normalized firing rate maps were generated by dividing the open field environment into 3-cm spatial bins. For each spatial bin, an occupancy-normalized firing rate was computed by dividing the total number of spikes falling into that bin by the total time the animal spent in that bin. Firing rate maps were then smoothed by a 3-cm wide two-dimensional Gaussian kernel.

Modulation of baseline firing rates by visual inputs.
In order to identify neurons, whose firing rates are modulated by the illumination of the environment (consistently either higher or lower firing rates during light or darkness), we computed the average firing rate for each light and dark epoch and tested if the differences between light epochs and the following dark epochs and the differences between dark epochs and the following light epochs reached statistical significance at alpha = 0.05 using Student's paired t-test. To analyze the time-course of changes in baseline firing rates after transition from light to dark or from dark to light, we first computed the peristimulus time histogram with 5-s binning around the transition point and then computed the average of z-scored firing rates across neurons.

Identification and classification of speed-modulated neurons. To identify speed modulated neurons in an unbiased way, we used a linear non-linear Poisson (LN) model (Hardcastle et al., 2017) which tested for significant modulation of firing rates by position, head

direction, LFP theta phase, and/or running speed (Fig. 4). For a robust analysis, we first screened for cells which showed stable firing across the whole recording session. Cells, whose mean firing rates were below 1-Hz or whose mean firing rates differed more than by a factor of two between the first and second halves of the recording session, were excluded from the analysis. Critically, we next adjusted for differences in the number of spikes between the light and dark conditions by randomly deleting spikes for the condition with more spikes. Such random deletion of spikes ensured that the statistical power to detect modulation of firing rates by running speed, position, head direction and/or theta phase was identical for the light and dark condition, and further ensured that differences in baseline firing rate between light and dark conditions did not affect the further analysis shown in Fig. 4. To compare speed modulation of firing rates on the population level, we clustered neurons into positively and negatively speed-modulated neurons using hierarchical clustering (clustergram, bioinformatics toolbox, MATLAB).

Grid score. The grid score was used as a measure of hexagonal symmetry of grid fields. The grid score was calculated as described in detail in Brandon et al. (2011) (gridness measure 3). In short, we computed the two-dimensional rate map autocorrelogram and computed correlations between this and rotated versions of itself after correction of elliptical eccentricity. If hexagonal symmetry is present, those correlations will peak at multiples of 60 degrees. The difference between the smallest peak and the largest trough was then defined as the grid score. Grid cells were defined as cells with a grid score > 0.85 in either light or dark condition.

Spatial information. We defined the spatial information as the delta entropy $\Delta H = H_{max} - H$. H_{max} is the maximal amount of randomness given by a completely random distribution of spike locations in the open field environment defined by $H_{max} = -\sum_{i=1}^{n} p * \log_2 p$, with $p = \frac{1}{n}$, where n is the number of spatial bins. H is the observed amount of randomness in the distribution of spike locations given by $H(X|spike) = -\sum_{i=1}^{n} p(x_i|spike) * \log_2 p(x_i|spike)$, where X is the animal's location, x_i is the ith spatial bin, n is the number of spatial bins and $p(x_i|spike)$ is the probability that $X = x_i$ when a spike is observed. ΔH can then be understood as an increase in the amount of order in the distribution of spike locations relative to a completely random (uniform) distribution of spike locations.

Spatial correlation. Firing rate map similarities were quantified by the spatial correlation between two firing rate maps. To compute the spatial correlation, the spatial bins of the firing rate maps were transformed into a single vector. The spatial correlation was then computed as the Pearson's correlation coefficient between two of those spatially binned firing rate vectors.

Spatiotemporal correlation. To analyze spatial stability of grid cell firing in the time domain, we used the firing rate map of the light condition to compute the expected firing rate for each of the 20-msec time bins of the animal's trajectory. We next computed the Pearson's correlation coefficient between the observed 20-msec binned firing rate and the expected 20-msec binned firing rate.

Experimental design and statistical analysis. Details on statistical analyses on each experiment are reported in the Results section. Statistical tests used in this study include Student's paired t-test and nonparametric statistical tests for repeated measures, namely Wilcoxon's signed rank test and Friedman's test. Posthoc testing was performed if the Friedman test yielded a significant result at alpha = 0.05.

Code accessibility. Custom MATLAB code used for data analysis can be found at https://github.com/hasselmonians or can be made available upon request. Violin plots were created using R software (R Core Team, 2019; R: A language and environment for statistical computing; R Foundation for Statistical Computing, Vienna, Austria).

ACKNOWLEDGMENTS

This work was supported by the National Institute of Mental Health, grant numbers R01 MH60013 and R01 MH120073, by the National Institute of Neurological Disorders and Stroke, grant number K99NS116129, and by the Office of Naval Research MURI N00014-16-1-2832 and N00014-19-1-2571, and Office of Naval Research DURIP N00014-17-1-2304.

COMPETING INTERESTS

None

REFERENCES

Barry, C., Hayman, R., Burgess, N., & Jeffery, K. J. (2007). Experience-dependent rescaling of entorhinal grids. *Nature Neuroscience*, *10*(6), 682–684. https://doi.org/10.1038/nn1905

Blair, H. T., Gupta, K., & Zhang, K. (2008). Conversion of a phase- to a rate-coded position signal by a three-stage model of theta cells, grid cells, and place cells. *Hippocampus*, *18*(12), 1239–1255. https://doi.org/10.1002/hipo.20509

Brandon, M. P., Bogaard, A. R., Libby, C. P., Connerney, M. A., Gupta, K., & Hasselmo, M. E. (2011). Reduction of theta rhythm dissociates grid cell spatial periodicity from directional tuning. *Science (New York, N.Y.)*, *332*(6029), 595–599. https://doi.org/10.1126/science.1201652

Burak, Y., & Fiete, I. R. (2009). Accurate path integration in continuous attractor network models of grid cells. *PLoS Computational Biology*, *5*(2), e1000291. https://doi.org/10.1371/journal.pcbi.1000291

Burgess, N. (2008). Grid cells and theta as oscillatory interference: Theory and predictions. *Hippocampus*, *18*(12), 1157–1174. https://doi.org/10.1002/hipo.20518

Burgess, N., Barry, C., & O'Keefe, J. (2007). An oscillatory interference model of grid cell firing. *Hippocampus*, *17*(9), 801–812. https://doi.org/10.1002/hipo.20327

Bush, D., & Burgess, N. (2014). A Hybrid Oscillatory Interference/Continuous Attractor Network Model of Grid Cell Firing. *Journal of Neuroscience*, *34*(14), 5065–5079. https://doi.org/10.1523/JNEUROSCI.4017-13.2014

Campbell, M. G., & Giocomo, L. M. (2018). Self-motion processing in visual and entorhinal cortices: Inputs, integration, and implications for position coding. *Journal of Neurophysiology*. https://doi.org/10.1152/jn.00686.2017

Campbell, M. G., Ocko, S. A., Mallory, C. S., Low, I. I. C., Ganguli, S., & Giocomo, L. M. (2018). Principles governing the integration of landmark and self-motion cues in entorhinal cortical codes for navigation. *Nature Neuroscience*, *21*(8), 1096–1106. https://doi.org/10.1038/s41593-018-0189-y

Chen, G., King, J. A., Lu, Y., Cacucci, F., & Burgess, N. (2018). Spatial cell firing during virtual navigation of open arenas by head-restrained mice. *ELife*, *7*. https://doi.org/10.7554/eLife.34789

Chen, G., Lu, Y., King, J. A., Cacucci, F., & Burgess, N. (2019). Differential influences of environment and self-motion on place and grid cell firing. *Nature Communications*, *10*(1), 630. https://doi.org/10.1038/s41467-019-08550-1

Chen, G., Manson, D., Cacucci, F., & Wills, T. J. (2016). Absence of Visual Input Results in the Disruption of Grid Cell Firing in the Mouse. *Current Biology: CB*. https://doi.org/10.1016/j.cub.2016.06.043

Cheung, A. (2016). Probabilistic Learning by Rodent Grid Cells. *PLoS Computational Biology*, *12*(10), e1005165. https://doi.org/10.1371/journal.pcbi.1005165

Chrobak, J. J., Stackman, R. W., & Walsh, T. J. (1989). Intraseptal administration of muscimol produces dose-dependent memory impairments in the rat. *Behavioral and Neural Biology*, *52*(3), 357–369.

Climer, J. R., DiTullio, R., Newman, E. L., Hasselmo, M. E., & Eden, U. T. (2015). Examination of rhythmicity of extracellularly recorded neurons in the entorhinal cortex. *Hippocampus*, *25*(4), 460–473. https://doi.org/10.1002/hipo.22383

Dannenberg, H., Kelley, C., Hoyland, A., Monaghan, C. K., & Hasselmo, M. E. (2019). The Firing Rate Speed Code of Entorhinal Speed Cells Differs across Behaviorally Relevant Time Scales and Does Not Depend on Medial Septum Inputs. *The Journal of Neuroscience*, *39*(18), 3434–3453. https://doi.org/10.1523/JNEUROSCI.1450-18.2019

Dannenberg, H., Pabst, M., Braganza, O., Schoch, S., Niediek, J., Bayraktar, M., Mormann, F., & Beck, H. (2015). Synergy of direct and indirect cholinergic septo-hippocampal pathways coordinates firing in hippocampal networks. *The Journal of Neuroscience*, *35*(22), 8394–8410. https://doi.org/10.1523/JNEUROSCI.4460-14.2015

Evans, T., Bicanski, A., Bush, D., & Burgess, N. (2016). How environment and self-motion combine in neural representations of space. *The Journal of Physiology*, *594*(22), 6535–6546. https://doi.org/10.1113/JP270666

Fuhrmann, F., Justus, D., Sosulina, L., Kaneko, H., Beutel, T., Friedrichs, D., Schoch, S., Schwarz, M. K., Fuhrmann, M., & Remy, S. (2015). Locomotion, Theta Oscillations, and the Speed-Correlated Firing of Hippocampal Neurons Are Controlled by a Medial Septal Glutamatergic Circuit. *Neuron*, *86*(5), 1253–1264. https://doi.org/10.1016/j.neuron.2015.05.001

Fuhs, M. C., & Touretzky, D. S. (2006). A spin glass model of path integration in rat medial entorhinal cortex. *The Journal of Neuroscience: The Official Journal of the Society for Neuroscience*, *26*(16), 4266–4276. https://doi.org/10.1523/JNEUROSCI.4353-05.2006

Fyhn, M., Hafting, T., Witter, M. P., Moser, E. I., & Moser, M.-B. (2008). Grid cells in mice. *Hippocampus*, *18*(12), 1230–1238. http://dx.doi.org/10.1002/hipo.20472

Fyhn, M., Molden, S., Witter, M. P., Moser, E. I., & Moser, M.-B. (2004). Spatial representation in the entorhinal cortex. *Science*, *305*(5688), 1258–1264. http://dx.doi.org/10.1126/science.1099901

Gil, M., Ancau, M., Schlesiger, M. I., Neitz, A., Allen, K., De Marco, R. J., & Monyer, H. (2018). Impaired path integration in mice with disrupted grid cell firing. *Nature Neuroscience*, *21*(1), 81–91. https://doi.org/10.1038/s41593-017-0039-3

Giocomo, L. M. (2016). Environmental boundaries as a mechanism for correcting and anchoring spatial maps. *The Journal of Physiology*, *594*(22), 6501–6511. https://doi.org/10.1113/JP270624

Givens, B., & Olton, D. S. (1994). Local modulation of basal forebrain: Effects on working and reference memory. *The Journal of Neuroscience*, *14*(6), 3578–3587.

Hafting, T., Fyhn, M., Molden, S., Moser, M.-B., & Moser, E. I. (2005). Microstructure of a spatial map in the entorhinal cortex. *Nature*, *436*(7052), 801–806. http://dx.doi.org/10.1038/nature03721

Hardcastle, K., Ganguli, S., & Giocomo, L. M. (2015). Environmental Boundaries as an Error Correction Mechanism for Grid Cells. *Neuron*, *86*(3), 827–839. https://doi.org/10.1016/j.neuron.2015.03.039

Hardcastle, K., Maheswaranathan, N., Ganguli, S., & Giocomo, L. M. (2017). A Multiplexed, Heterogeneous, and Adaptive Code for Navigation in Medial Entorhinal Cortex. *Neuron*, *94*(2), 375-387.e7. https://doi.org/10.1016/j.neuron.2017.03.025

Hasselmo, M. E. (2008). Grid cell mechanisms and function: Contributions of entorhinal persistent spiking and phase resetting. *Hippocampus*, *18*(12), 1213–1229. https://doi.org/10.1002/hipo.20512

Hinman, J. R., Brandon, M. P., Climer, J. R., Chapman, G. W., & Hasselmo, M. E. (2016). Multiple Running Speed Signals in Medial Entorhinal Cortex. *Neuron*, *91*(3), 666–679. https://doi.org/10.1016/j.neuron.2016.06.027

Hinman, J. R., Penley, S. C., Long, L. L., Escabí, M. A., & Chrobak, J. J. (2011). Septotemporal variation in dynamics of theta: Speed and habituation. *Journal of Neurophysiology*, *105*(6), 2675–2686. https://doi.org/10.1152/jn.00837.2010

Jacob, P.-Y., Capitano, F., Poucet, B., Save, E., & Sargolini, F. (2019). Path integration maintains spatial periodicity of grid cell firing in a 1D circular track. *Nature Communications*, *10*(1), 1–13. https://doi.org/10.1038/s41467-019-08795-w

Jacob, P.-Y., Gordillo-Salas, M., Facchini, J., Poucet, B., Save, E., & Sargolini, F. (2017). Medial entorhinal cortex and medial septum contribute to self-motion-based linear distance estimation. *Brain Structure & Function*, *222*(6), 2727–2742. https://doi.org/10.1007/s00429-017-1368-4

Jacob, P.-Y., Poucet, B., Liberge, M., Save, E., & Sargolini, F. (2014). Vestibular control of entorhinal cortex activity in spatial navigation. *Frontiers in Integrative Neuroscience*, *8*, 38. https://doi.org/10.3389/fnint.2014.00038

Justus, D., Dalügge, D., Bothe, S., Fuhrmann, F., Hannes, C., Kaneko, H., Friedrichs, D., Sosulina, L., Schwarz, I., Elliott, D. A., Schoch, S., Bradke, F., Schwarz, M. K., & Remy, S. (2016). Glutamatergic synaptic integration of locomotion speed via septoentorhinal projections. *Nature Neuroscience*. https://doi.org/10.1038/nn.4447

Koenig, J., Linder, A. N., Leutgeb, J. K., & Leutgeb, S. (2011). The spatial periodicity of grid cells is not sustained during reduced theta oscillations. *Science (New York, N.Y.)*, *332*(6029), 592–595. https://doi.org/10.1126/science.1201685

Kraus, B. J., Brandon, M. P., Robinson, R. J., Connerney, M. A., Hasselmo, M. E., & Eichenbaum, H. (2015). During Running in Place, Grid Cells Integrate Elapsed Time and Distance Run. *Neuron*, *88*(3), 578–589. https://doi.org/10.1016/j.neuron.2015.09.031

Kropff, E., Carmichael, J. E., Moser, M.-B., & Moser, E. I. (2015). Speed cells in the medial entorhinal cortex. *Nature*, *523*(7561), 419–424. https://doi.org/10.1038/nature14622

Krupic, J., Bauza, M., Burton, S., Barry, C., & O'Keefe, J. (2015). Grid cell symmetry is shaped by environmental geometry. *Nature*, *518*(7538), 232–235. https://doi.org/10.1038/nature14153

Lawson, V. H., & Bland, B. H. (1993). The role of the septohippocampal pathway in the regulation of hippocampal field activity and behavior: Analysis by the intraseptal microinfusion of carbachol, atropine, and procaine. *Experimental Neurology*, *120*(1), 132–144. https://doi.org/10.1006/exnr.1993.1047

McNaughton, B. L., Battaglia, F. P., Jensen, O., Moser, E. I., & Moser, M.-B. (2006). Path integration and the neural basis of the "cognitive map". *Nat Rev Neurosci*, *7*(8), 663–678. http://dx.doi.org/10.1038/nrn1932

Munn, R. G. K., Mallory, C. S., Hardcastle, K., Chetkovich, D. M., & Giocomo, L. M. (2020). Entorhinal velocity signals reflect environmental geometry. *Nature Neuroscience*, *23*(2), 239–251. https://doi.org/10.1038/s41593-019-0562-5

Oostenveld, R., Fries, P., Maris, E., & Schoffelen, J.-M. (2011). FieldTrip: Open source software for advanced analysis of MEG, EEG, and invasive electrophysiological data. *Computational Intelligence and Neuroscience*, *2011*, 156869. https://doi.org/10.1155/2011/156869

Pérez-Escobar, J. A., Kornienko, O., Latuske, P., Kohler, L., & Allen, K. (2016). Visual landmarks sharpen grid cell metric and confer context specificity to neurons of the medial entorhinal cortex. *ELife*, *5*. https://doi.org/10.7554/eLife.16937

Raudies, F., Brandon, M. P., Chapman, G. W., & Hasselmo, M. E. (2015). Head direction is coded more strongly than movement direction in a population of entorhinal neurons. *Brain Research*, *1621*, 355–367. https://doi.org/10.1016/j.brainres.2014.10.053

Raudies, F., & Hasselmo, M. E. (2015). Differences in Visual-Spatial Input May Underlie Different Compression Properties of Firing Fields for Grid Cell Modules in Medial Entorhinal Cortex. *PLoS Computational Biology*, *11*(11), e1004596. https://doi.org/10.1371/journal.pcbi.1004596

Raudies, F., Mingolla, E., & Hasselmo, M. E. (2012). Modeling the influence of optic flow on grid cell firing in the absence of other cues1. *Journal of Computational Neuroscience*, *33*(3), 475–493. https://doi.org/10.1007/s10827-012-0396-6

Sargolini, F., Fyhn, M., Hafting, T., McNaughton, B. L., Witter, M. P., Moser, M.-B., & Moser, E. I. (2006). Conjunctive representation of position, direction, and velocity in entorhinal cortex. *Science (New York, N.Y.)*, *312*(5774), 758–762. https://doi.org/10.1126/science.1125572

Sreenivasan, S., & Fiete, I. (2011). Grid cells generate an analog error-correcting code for singularly precise neural computation. *Nature Neuroscience*, *14*(10), 1330–1337. https://doi.org/10.1038/nn.2901

Taube, J. S. (2007). The Head Direction Signal: Origins and Sensory-Motor Integration. *Annual Review of Neuroscience*, *30*(1), 181–207. https://doi.org/10.1146/annurev.neuro.29.051605.112854

Taube, J. S., Muller, R. U., & Ranck, J. B. (1990a). Head-direction cells recorded from the postsubiculum in freely moving rats. II. Effects of environmental manipulations. *The Journal of Neuroscience*, *10*(2), 436–447.

Taube, J. S., Muller, R. U., & Ranck, J. B. (1990b). Head-direction cells recorded from the postsubiculum in freely moving rats. II. Effects of environmental manipulations. *The Journal of Neuroscience: The Official Journal of the Society for Neuroscience*, *10*(2), 436–447.

Tennant, S. A., Fischer, L., Garden, D. L. F., Gerlei, K. Z., Martinez-Gonzalez, C., McClure, C., Wood, E. R., & Nolan, M. F. (2018). Stellate Cells in the Medial Entorhinal Cortex Are

Required for Spatial Learning. *Cell Reports*, *22*(5), 1313–1324. https://doi.org/10.1016/j.celrep.2018.01.005

Winter, S. S., Mehlman, M. L., Clark, B. J., & Taube, J. S. (2015). Passive Transport Disrupts Grid Signals in the Parahippocampal Cortex. *Current Biology: CB*, *25*(19), 2493–2502. https://doi.org/10.1016/j.cub.2015.08.034

Zilli, E. A., & Hasselmo, M. E. (2010). Coupled Noisy Spiking Neurons as Velocity-Controlled Oscillators in a Model of Grid Cell Spatial Firing. *Journal of Neuroscience*, *30*(41), 13850–13860. https://doi.org/10.1523/JNEUROSCI.0547-10.2010

FIGURES

Figure 1

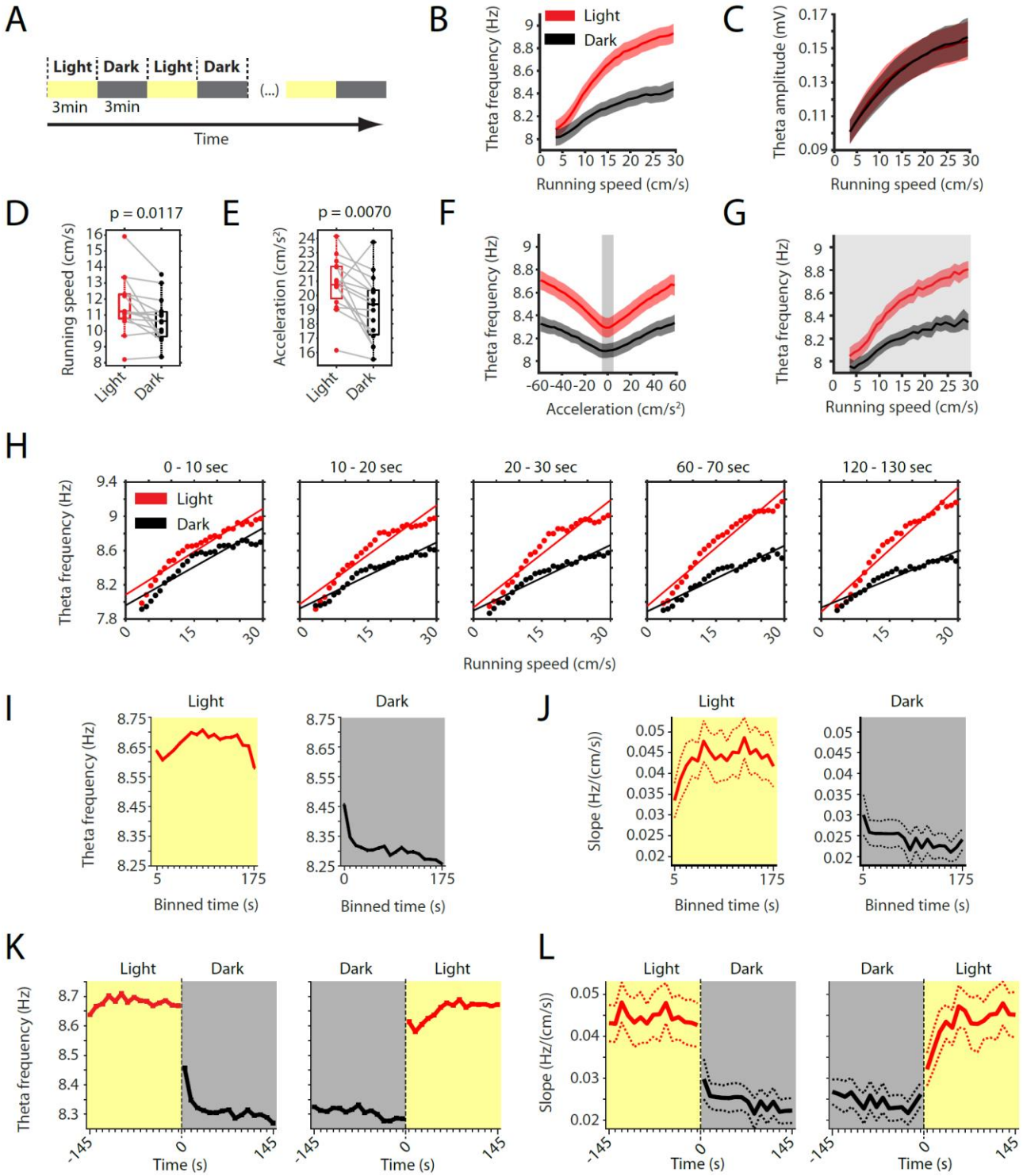

Figure 1. Speed signal by local field potential theta frequency decreases in darkness. A, Experimental paradigm. Local field potential (LFP) theta oscillatory activity was recorded in mice freely foraging in a 1-m square open field environment containing a visual cue card during alternating epochs of illumination by a ceiling light (light) and complete darkness (dark). A typical recording lasted 42-min with 3-min alternating light and dark epochs. **B,** Plot of theta frequency vs. running speed shows that the slope of the relationship decreases during darkness. Solid lines show the mean, shaded area show the s.e.m. for n = 15 mice. Data on the light condition are shown in red, data on the dark condition are shown in black and grey. **C,** Same as in B, but for theta amplitude. **D,** Running speed decreases slightly during darkness. Each data point shows the mean value for one mouse, box plots show mean, 25th and 75th percentiles, grey lines connect data from the same mouse; t = 2,90, df = 14, p = 0.0117, Student's paired t-test. **E,** Running acceleration decreases slightly during darkness. Data visualization as in D; t = 3.16, df = 14, p = 0.0070, Student's paired t-test. **F,** LFP theta frequency vs. running acceleration relationship is reduced for all acceleration values in complete darkness. Grey background highlights the interval of acceleration values between -5 cm/s^2 and 5 cm/s^2. **G,** LFP theta frequency vs. running speed relationship based on the subset of time points where the running acceleration is near zero in the interval shown in F between -5 cm/s^2 and 5 cm/s^2. **H-L,** Figure panels show sequential 10-sec bins of LFP data after transitions between light and dark. Each data point shows the mean across all epochs of the same condition (light or dark) from 73 recording sessions from 13 mice. Yellow background indicates the light condition; grey background indicates the dark condition. **H,** Theta frequency speed tuning curves for subsequent 10-sec blocks after transitions between light and dark. Straight lines are the linear regression lines to the data. **I,** Data points (with errorbars) show the mean (± s.e.m.) of theta frequency for the first three minutes in light and dark summed over data from all mice in 10-sec bins (errorbars are within the line width). **J,** Solid and dashed lines show the means and 95% confidence intervals of the slopes of the theta frequency vs. running speed relationships for sequential 10-sec bins for the first three minutes in light and dark; same visualization scheme as in I. **K,** Left and right panels show 10-sec binned mean ± s.e.m of theta frequency around the transition points from light to dark and from dark to light, respectively (errorbars are within the line width). **L,** Left and right panels show 10-sec binned peristimulus time histograms of the slopes of the theta frequency vs. running speed relationships around the transition points from light to dark and dark to light, respectively. Solid and dashed lines show means and 95% confidence intervals. Same visualization scheme as in K.

Figure 2

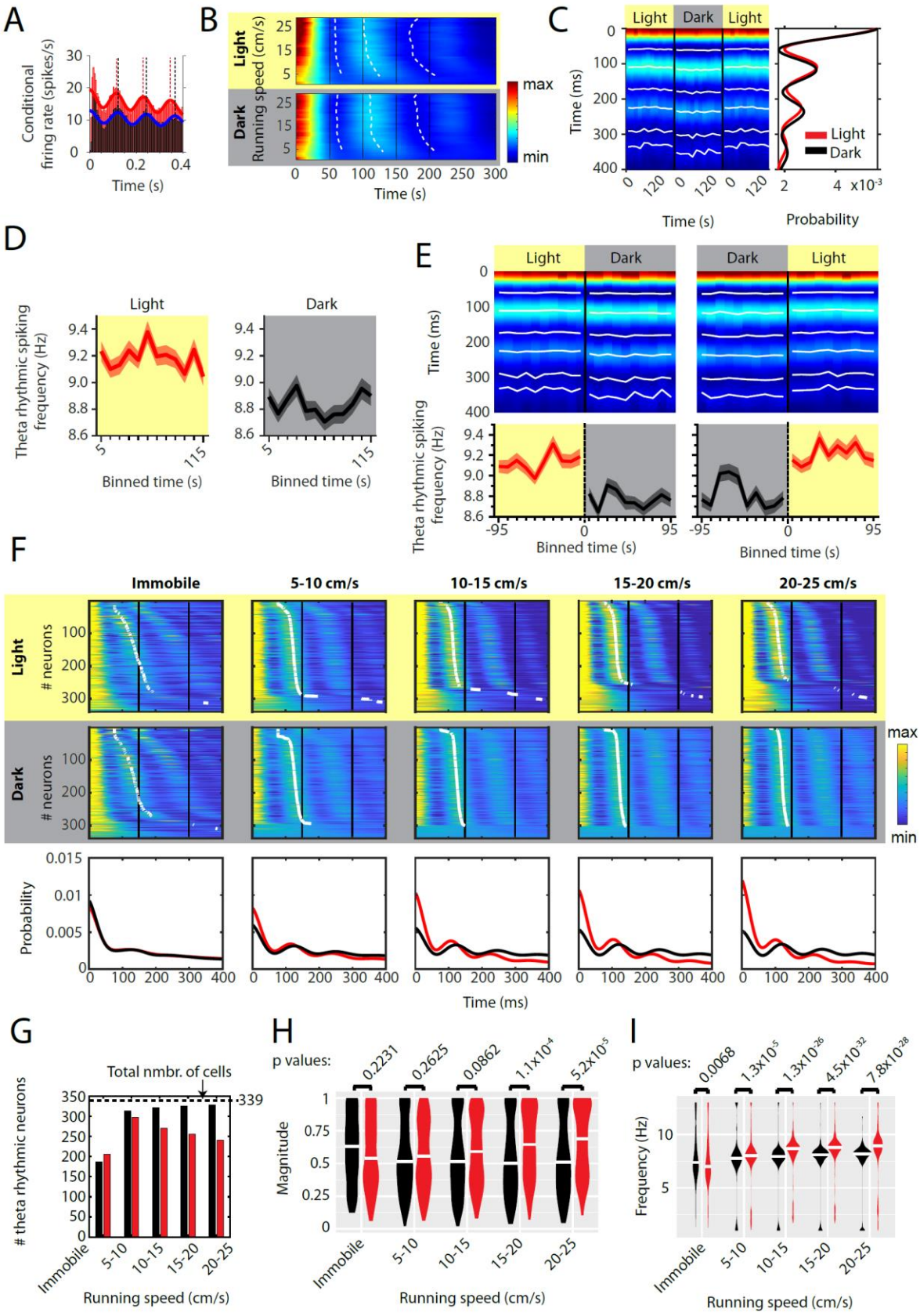
A
Conditional firing rate (spikes/s)
Time (s)
B
Light
Dark
Running speed (cm/s)
max
min
Time (s)
C
Light
Dark
Light
Time (ms)
Time (s)
Probability
x10^-3
D
Light
Dark
Theta rhythmic spiking frequency (Hz)
Binned time (s)
E
Light
Dark
Dark
Light
Time (ms)
Theta rhythmic spiking frequency (Hz)
Binned time (s)
F
Immobile
5-10 cm/s
10-15 cm/s
15-20 cm/s
20-25 cm/s
Light
Dark
neurons
max
min
Probability
Time (ms)
G
Total nmbr. of cells
339
theta rhythmic neurons
Immobile
5-10
10-15
15-20
20-25
Running speed (cm/s)
H
p values:
0.2231
0.2625
0.0862
1.1x10^-4
5.2x10^-5
Magnitude
Running speed (cm/s)
I
p values:
0.0068
1.3x10^-5
1.3x10^-26
4.5x10^-32
7.8x10^-28
Frequency (Hz)
Running speed (cm/s)

Figure 2. Changes in theta rhythmic firing with running speed are differentially affected by visual inputs. Red color and/or yellow background indicate data on the light condition, black and grey color and/or grey background indicate data on the dark condition. Figures show data from theta rhythmic neurons from a total of 14 mice. **A,** Autocorrelogram of one example neuron showing theta rhythmic firing in light and dark. Solid lines show the MLE model of the data (see Methods). Dashed lines indicate the positions of the peaks in the autocorrelogram. Larger lags between peaks translate into a lower frequency of theta rhythmic firing. **B,** Figure shows color-coded mean autocorrelogram fits across neurons per running speed bin. Speed bins range from 1 ±4 cm/s cm/s to 29 ±4 cm/s (see Methods). Upper panel shows data for the light condition, lower panel shows data for the dark condition. Dashed white line connects the first peaks in the mean autocorrelogram models. n = 340 neurons. **C,** Left panel shows the color-coded mean autocorrelogram models averaged across neurons for sequential 10-sec time bins of data for all light epochs and dark epochs. Solid white lines show the peaks and troughs in the autocorrelogram models. Data on the light condition are duplicated for better visualization. Right panel shows the averages of autocorrelogram models across neurons and across 10-sec time bins comparing light vs. dark. n = 342 neurons. **D,** Time course of the mean theta rhythmic firing frequency across neurons for sequential 10-sec time bins in the light and dark conditions. Data are plotted as mean ± s.e.m; n = 342 neurons. **E,** Left and right panels show data on the transition periods from light to dark and dark to light, respectively. Upper panels show color-coded mean autocorrelogram models per 10-sec bins before and after the transition point. White lines mark the peaks and troughs in the autocorrelogram models. Lower panels show the theta rhythmic firing frequency averaged across neurons for sequential 10-sec time bins before and after the transition point. n = 342 neurons. **F,** Upper panels show the color coded MLE autocorrelogram models for each neuron and different running speeds. Immobility was defined as running speed < 3 cm/s. Neurons are sorted per condition in order of their theta rhythmic firing frequency. White points indicate the first peak of the autocorrelogram fit in neurons showing statistically significant theta modulation in the corresponding condition at alpha = 0.1. Lower row shows the average across autocorrelogram models per condition. Note that higher synchrony across neurons results in higher rhythmicity magnitude in the average across neurons, n = 339. **G**, Number of neurons shown in F with statistically significant spiking rhythmicity at alpha = 0.1 determined by the MLE model (see Methods) for different running speeds in light and dark. **H,** Violin plots show the distribution of theta rhythmicity magnitudes of neurons in G for different running speeds comparing light and dark conditions. Numbers show

the p-values for Kolmogorov-Smirnov tests comparing data between light and dark. See Results for number of neurons per condition. **I,** Same as H, but for theta rhythmic firing frequency.

Figure 3

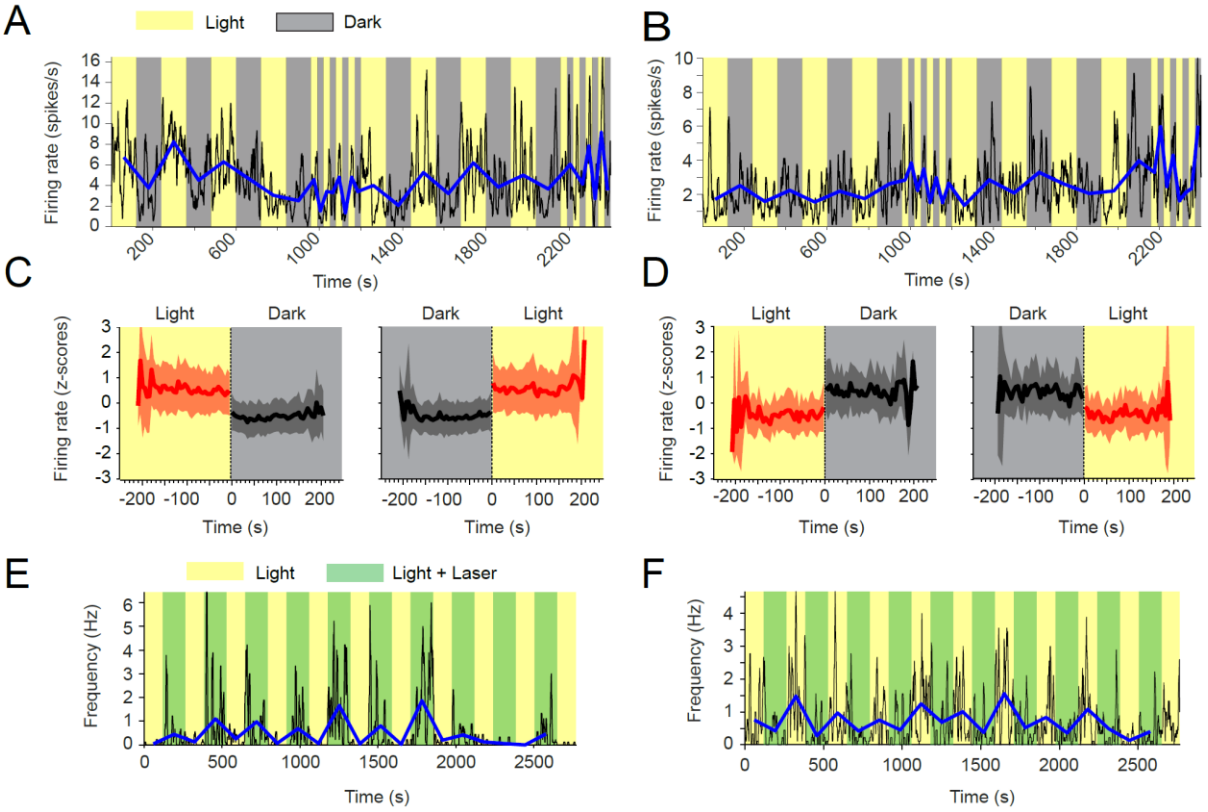

Figure 3. Visual inputs alter baseline firing rates of neurons in the medial entorhinal cortex. A-D, Yellow background indicates duration of light epochs, grey background indicates duration of dark epochs. **A,** Data on firing rate from one example neuron in the medial entorhinal cortex (MEC) with its baseline firing rate negatively modulated by darkness. Black lines show the firing rate at 1-s resolution. Blue lines show the average firing rate per light or dark epoch. **B,** Data on firing rate from one example neuron in the MEC, whose baseline firing rate is positively modulated by darkness; same visualization scheme as in A. **C,** Left and right panels show the mean z-scored firing rate across n = 139 neurons with significantly negative modulation of firing rates by darkness (see Methods) in 5-s bins around the transition point from light to dark and dark to light, respectively. Red color indicates data from the light condition, black and grey color indicate data from the dark condition. Solid lines and shaded areas show mean and SD. **D,** Same as C, but for neurons with positive modulation of baseline firing rates by darkness; n = 32. **E, F,** Yellow background indicates light condition, green background indicates the presence of an egocentrically stable spot of green laser light above the animal's head during the standard light condition. **E,** Data on one example neuron in the MEC showing positive modulation of baseline firing rate in presence of the green laser light spot. Same visualization scheme as in A and C. **F,** As in E, but for one example neuron with negative modulation of baseline firing rate.

Figure 4

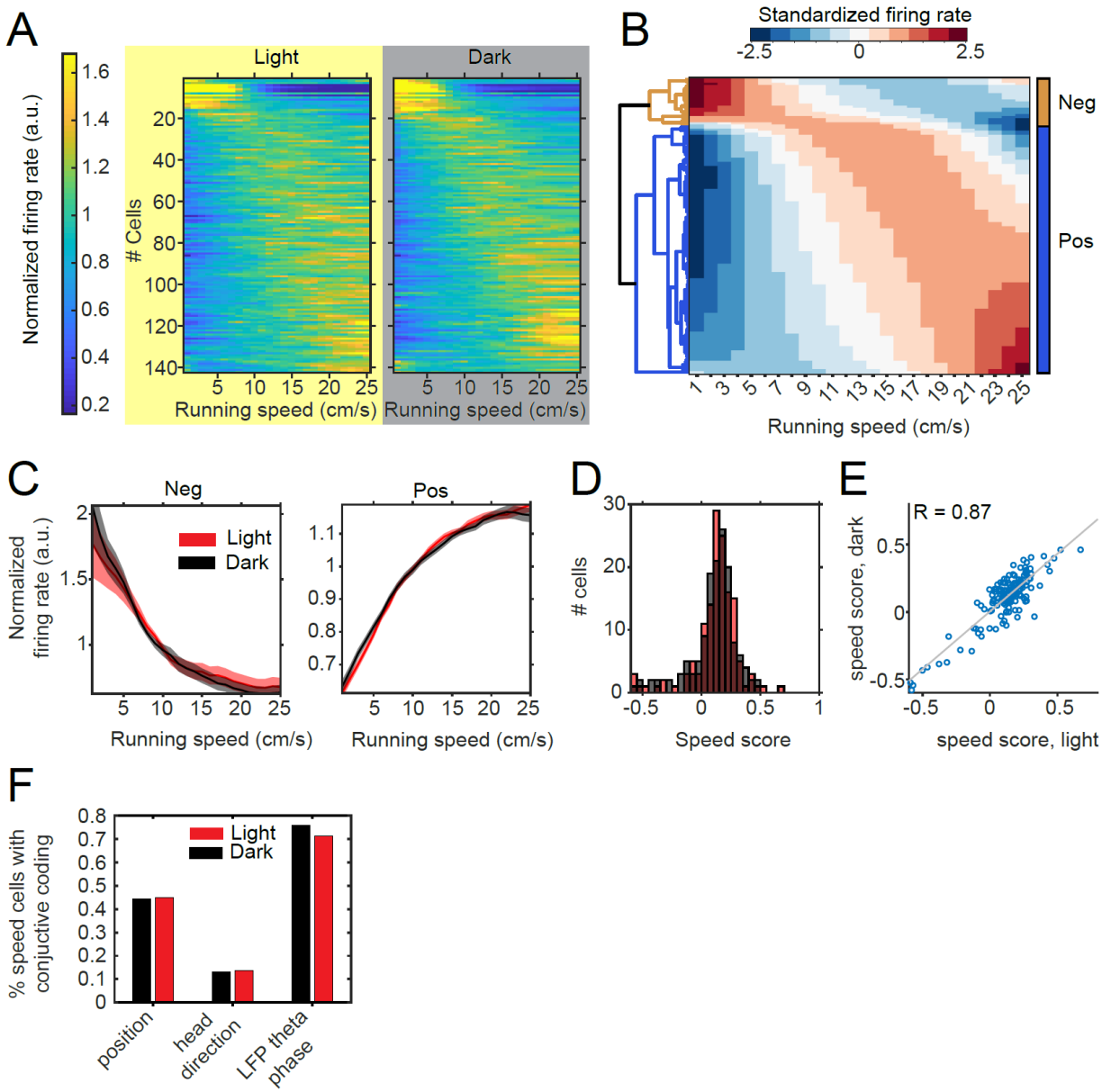

Figure 4. Speed modulation of firing rates is maintained in the absence of visual inputs. **A,** Left and right panels show speed response curves for the n = 142 neurons passing statistical significance of speed modulation in the LN-model (see Methods) for either the light or dark condition, respectively. For comparison of speed modulation across neurons and between light and dark conditions, firing rates were normalized and cells are plotted in the same order for light and dark. Cells were sorted by the location of peak firing on the running speed axis averaged across light and dark conditions. **B,** Clustergram visualizing the results of the hierarchical clustering of neurons by similarity of speed modulation of firing rates. The clustering was performed on the neurons' average speed response curves across light and dark conditions. **C,**

Left and right panels show speed response curves of negatively (n = 19) and positively (n = 123) modulated neurons; solid lines and shaded areas show mean ± s.e.m across neurons. **D,** Histogram of speed scores for all neurons showing significant speed modulation in either the light or dark condition. Red and grey color indicates data on light and dark, respectively. **E,** Scatter plot on same data shown in D comparing speed scores during the light with speed scores during the dark condition. **F,** Percentage of cells showing conjunctive coding of running speed and either position, head direction, or LFP theta phase (spike-phase locking) during the light and dark condition.

Figure 5

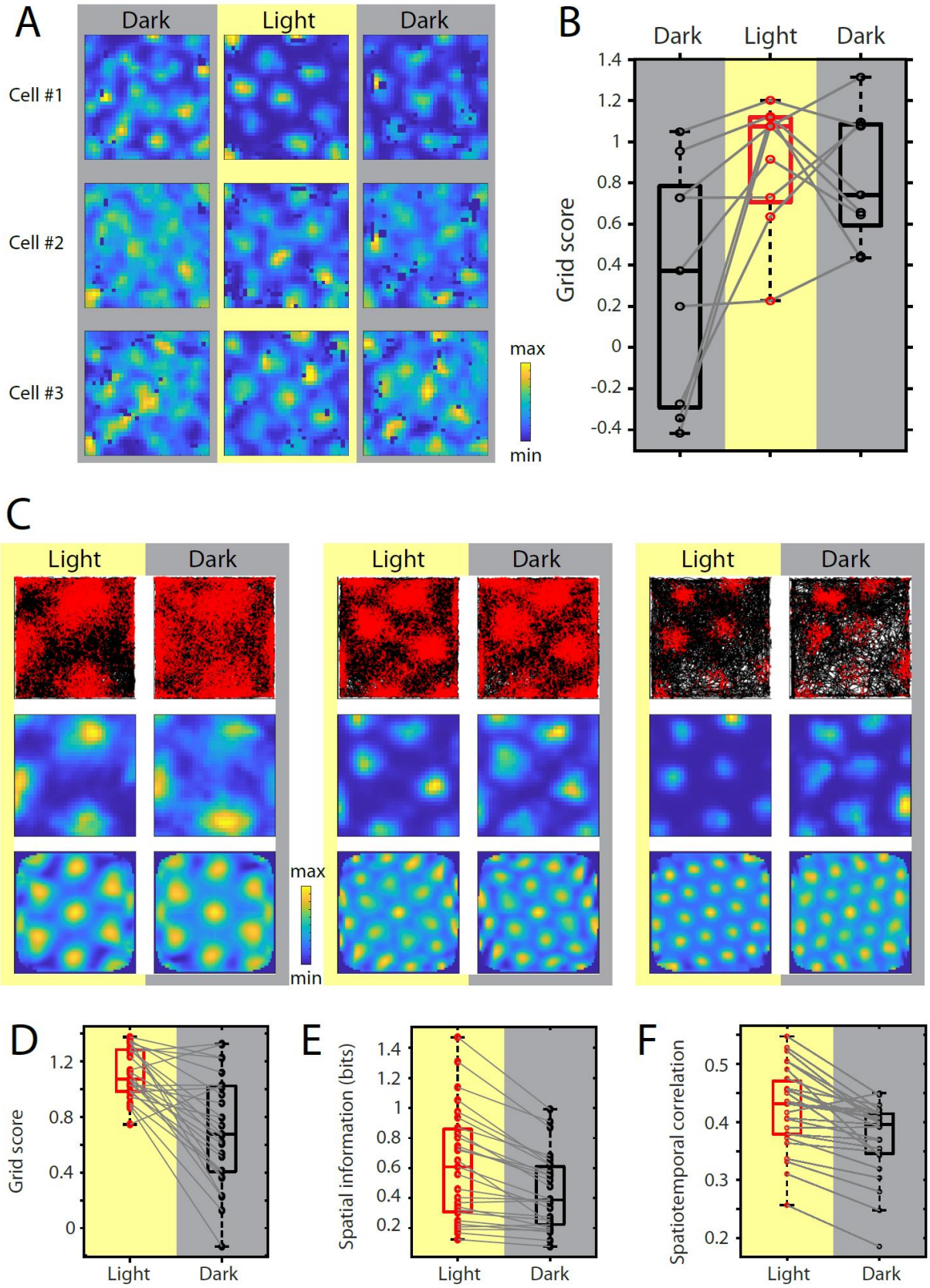
A
Dark
Light
Dark
Cell #1
Cell #2
Cell #3
max
min
B
Dark
Light
Dark
Grid score
1.4
1.2
1
0.8
0.6
0.4
0.2
0
-0.2
-0.4
C
Light
Dark
Light
Dark
Light
Dark
max
min
D
Grid score
1.2
0.8
0.4
0
Light
Dark
E
Spatial information (bits)
1.4
1.2
1
0.8
0.6
0.4
0.2
Light
Dark
F
Spatiotemporal correlation
0.5
0.4
0.3
0.2
Light
Dark

Figure 5. Grid cell spatial firing is maintained, but less stable in the absence of visual inputs. A, Firing rate maps of three example neurons during sequential dark, light, and dark sessions of 10-20 min duration. In the initial dark session, the animal was introduced to the open field environment in complete darkness. **B,** Box plots of grid scores during sequential dark, light, and dark session, n = 9 neurons from two mice. Black color and grey background indicate data on dark conditions, red color and yellow background indicate data on the light condition. Solid grey lines connect data points from the same grid cell. Chi-square = 10.89, p = 0.0043, Friedman's test; post-hoc tests revealed significant differences between the initial dark and light sessions as well as the initial dark and second dark sessions at alpha = 0.05. **C,** Top, middle, and bottom rows show trajectory plots, firing rate maps, and spatial autocorrelations of firing rate maps for three example grid cells recorded over multiple days during alternating light and dark epochs. Solid black lines in the trajectory plot show the trajectory of the animal, red dots mark the location of spikes during that trajectory. **D-E,** Box plots of grid scores, spatial information, and spatiotemporal correlation during light and dark; grey solid lines connect data points from the same grid cells; $p = 7.4 \times 10^{-5}$, $p = 9.8 \times 10^{-6}$, and $p = 2.4 \times 10^{-5}$; n = 27, Wilcoxon's signed rank test.

Figure 6

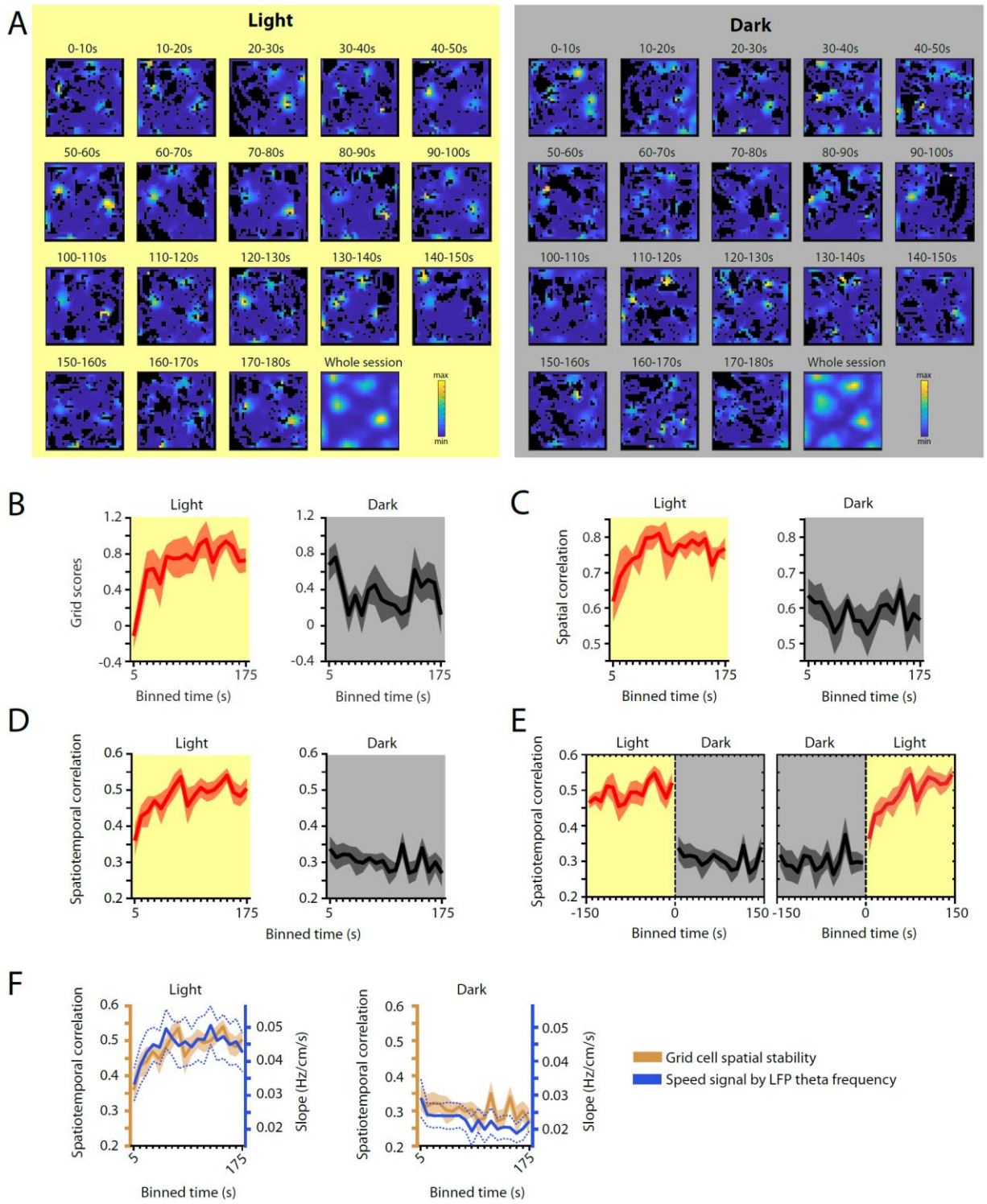
A
Light
Dark
0-10s
10-20s
20-30s
30-40s
40-50s
50-60s
60-70s
70-80s
80-90s
90-100s
100-110s
110-120s
120-130s
130-140s
140-150s
150-160s
160-170s
170-180s
Whole session
max
min
B
Light
Dark
Grid scores
Binned time (s)
C
Spatial correlation
D
Spatiotemporal correlation
E
F
Slope (Hz/cm/s)
Grid cell spatial stability
Speed signal by LFP theta frequency

Figure 6. Changes in grid cell spatial stability due to changes in visual inputs has a slow exponential component at a behavioral time scale and correlates with changes in the speed signal by local field potential theta frequency. A, Firing rate maps for sequential 10-sec bins of data after transitioning from dark to light (left side, yellow background) and light to dark (right side, grey background) for one example neuron. **B-D,** Time course measured in 10-sec bins of grid scores (B), spatial correlation (C), and spatiotemporal correlation (D) during the first three minutes of light and dark sessions. Solid lines show mean firing rates, shaded area indicates s.e.m.; n = 27 cells from three mice. **E,** Left and right panels show 10-sec binned data on spatiotemporal correlation around the transition points from light to dark and dark to light, respectively. Solid lines and shaded area show mean ± s.e.m.; n =27 grid cells from three mice. **F,** Overlay of data shown in Figures 6D and 1J showing the temporal alignment of changes in the slope of the theta frequency vs. running speed relationship (blue colors) and the spatial stability of grid cell firing measured by the spatiotemporal correlation (ocher colors). Left and right panels show data on first three minutes in the light and dark conditions, respectively.